Time-domain source parameter estimation of M_w 3–7 earthquakes in Japan from a large database of moment-rate functions

Keisuke Yoshida[1] and Hiroo Kanamori[2]

[1] Research Center for Prediction of Earthquakes and Volcanic Eruptions, Graduate School of Science, Tohoku University, Sendai, Japan

[2] Seismological Laboratory, California Institute of Technology, Pasadena, CA, 91125, USA

Abbreviated title: Time-domain source parameter estimation

Corresponding author: Keisuke Yoshida, Research Center for Prediction of Earthquakes and Volcanic Eruptions, Tohoku University, 6-6 Aza-Aoba, Aramaki, Aoba-Ku, Sendai, 980-8578, Japan (keisuke.yoshida.d7@tohoku.ac.jp), Tel: +81-22-795-6779, Fax: +81-22-264-3292

Summary

Time-domain analyses of seismic waveforms have revealed diverse source complexity in large earthquakes (M_w>7). However, source characteristics of small earthquakes have been studied by assuming a simple rupture pattern in the frequency domain. This study utilized high-quality seismic network data from Japan to systematically address the source complexities and radiated energies of M_w 3–7 earthquakes in the time domain. We first determined the apparent moment-rate functions (AMRFs) of the earthquakes using the empirical Green's functions. Some of the AMRFs showed multiple peaks, suggesting complex ruptures at multiple patches. We then estimated the radiated energies (E_R) of 1736 events having more than ten reliable AMRFs. The scaled energy (e_R=E_R/M_0) did not strongly depend on the seismic moment (M_0), focal mechanisms, or depth. The median value of e_R was 3.7×10^{-5}, which is comparable to those of previous studies; however, e_R varied by approximately one order of magnitude among earthquakes. Additionally, we measured the source complexity based on the radiated energy enhancement factor ($REEF$). The values of $REEF$ differed among earthquakes, implying diverse source complexity. The values of $REEF$ did not show strong scale dependence for M_w 3–7 earthquakes, suggesting that the source diversity of smaller earthquakes is similar to that of larger earthquakes at their representative spatial scales. Applying a simple spectral model (e.g., the ω^2-source model) to complex ruptures may produce substantial estimation errors of source parameters.

1. Introduction

Studies on the spatiotemporal evolution of large (M_w >7) earthquakes have significantly contributed to our understanding of earthquake rupture physics and diversity in different tectonic environments. Most of these studies have been made by time-domain analyses of seismic waveforms.

For small earthquakes (M_w <5), however, it is often difficult to resolve details of the rupture pattern; thus characterizing an earthquake source using several parameters is common, such as the seismic moment (M_0), radiated energy (E_R), stress drop ($\Delta\sigma$), rupture duration (T), spectral corner frequency (f_c), directivity, and complexity. In principle, these parameters can be estimated from the analysis of seismic waveforms on either the time domain or frequency domain. Since Brune (1970) developed a simple frequency-domain method, many studies have been made to establish various scaling relations (e.g., Allmann & Shearer 2009), as recently reviewed by Abercrombie (2021).

The corner frequency of the amplitude displacement spectrum, f_c, is used to estimate the rupture duration, T, and stress drop, $\Delta\sigma$. In most cases, the spatial dimension is only indirectly estimated from the corner frequency based on the assumption that the corner frequency is inversely proportional to the spatial dimension. This assumption is valid when the source time function has a simple pulse-like waveform. However, if the rupture pattern is complex, the relationship between the corner frequency and the source dimension is non-unique, and its relationship to the stress drop is ambiguous (e.g., Beresnev 2001). If the phase spectrum is used together with the amplitude spectrum, this ambiguity may be eliminated. However, few studies include the phase spectrum in their analysis because it is generally cumbersome.

To overcome this difficulty, we apply a time-domain method to high-quality seismic network

data from Japan, with the hope that we can systematically characterize the source properties of M_w 3 to 7 earthquakes. The issues in analysing small earthquakes in the time domain arises from the difficulty in obtaining reliable Green's functions at high frequencies. However, with the good seismic network data in Japan, we can estimate reliable apparent moment-rate functions (AMRFs) for small earthquakes (M_w>3) using empirical Green's functions (eGF) (Yoshida 2019). Here, we first created a database of AMRFs of many (~1700) earthquakes, and then systematically examined the relationships between various source parameters.

2. Data and Method

2.1. Earthquakes and waveform data

We applied a time-domain analysis to the earthquakes for which the moment tensors are listed in the F-net moment tensor catalogue (Fukuyama et al. 1998). We targeted crustal events on land from 2003 to 2021 that were surrounded by seismic networks (Fig. 1). Their moment magnitude M_w ranged from 3.0 to 7.0. We obtained velocity waveform data from the stations of national universities, Japan Meteorological Agency (JMA), and Hi-net (NIED, 2019a), F-net (NIED, 2019b), and V-net (NIED, 2019c) of the National Research Institute for Earth Science and Disaster Resilience (NIED) (Fig. 1b). Additionally, we obtained acceleration waveform data from the downhole acceleration sensors of the NIED KiK-net (NIED, 2019d), which are collocated with the Hi-net velocity sensors. Velocity waveform data were used to analyse M_w<5.5 earthquakes, whereas acceleration waveform data were used to analyse $M_w \geq 4.5$ earthquakes. Earthquakes with M_w 4.5–5.5 were analysed with both data sets separately. Yoshida (2019) estimated the AMRFs in this region in a preliminary study of M_w 3–5 earthquakes from 2004 to 2019. In this study, we expanded the data period, magnitude range, and analysed frequency range and implemented new quality control for AMRFs.

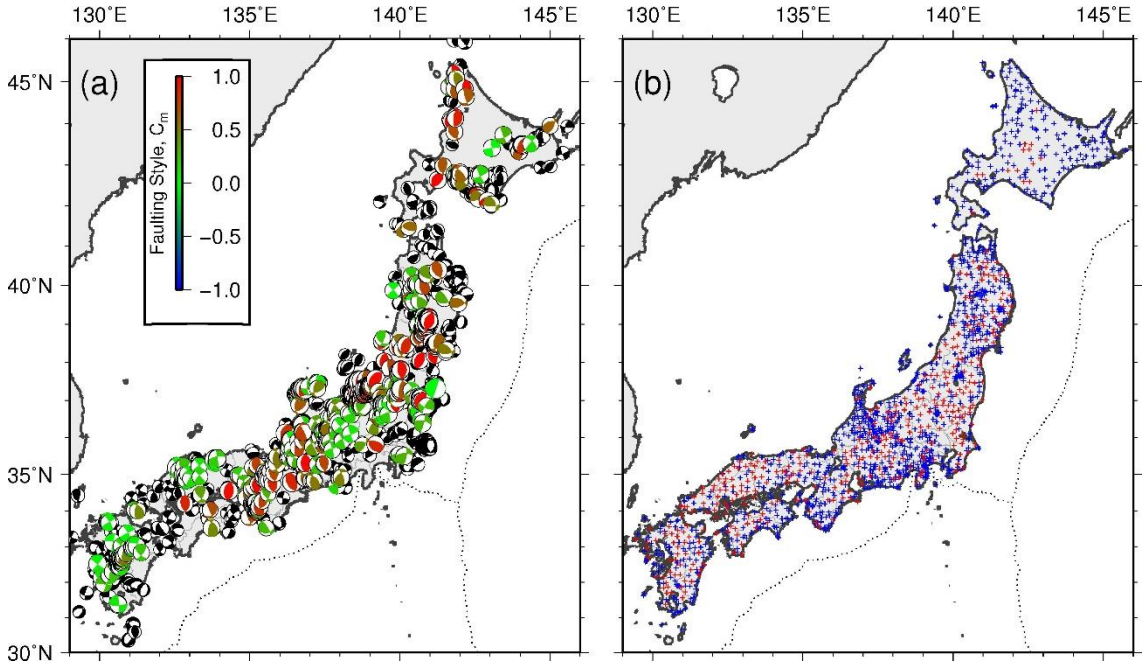

Figure 1. Earthquake data and seismic stations. (a) Earthquakes (M_w 3-7 in the crust of land areas) from the F-net moment tensor catalogue from March 2003 to May 2021. The earthquakes for which more than ten AMRFs were derived are coloured according to their faulting style. (b) Seismic stations. Blue crosses denote the stations with only velocity seismometers, and red triangles denote the stations with both velocity seismometers and accelerometers (KiK-net and Hi-net stations).

We used SH waves observed at stations within 100 km of the target earthquakes. The waveforms beginning 2.0 seconds before the arrival of the S-wave and lasting 10 s to 120 s, depending on the magnitude, were used. We used the arrival time of the S-wave listed in the JMA unified catalogue, if available. Otherwise, we computed the arrival time assuming the one-dimensional velocity structure of Ueno et al. (2002), which is routinely used to determine the hypocentres in the JMA unified catalogue.

We estimated the AMRFs of the target events using the waveforms of nearby smaller earthquakes (eGF events) to correct for the site and path effects (Hartzell 1978). These eGF events

satisfied the following two criteria: (1) the hypocentral distance from the target event was < 3.0 km according to the JMA unified catalogue, and (2) the magnitude was 1–2 magnitude units less than the target earthquake. Each target earthquake could have multiple eGF events.

2.2. Estimation of AMRFs

We determined each AMRF by deconvolving the observed waveforms with the eGFs at the same station, using the deconvolution algorithm developed by Ligorria & Ammon (1999) that employs the method of Kikuchi & Kanamori (1982). The moment-rate function was constrained to be positive in this inversion. All the basic analyses were performed on the time domain; however, we decided the frequency band and corrected for the estimated E_R with the widely-used ω^2-source model.

To perform stable deconvolution, we first applied a low-pass filter to the seismograms. The cut-off frequency of this filter, f_l, depends on the signal-to-noise (SN) ratio of the seismograms. For a given seismogram, f_l should be as high as possible to obtain an accurate E_R while maintaining good deconvolution stability. To treat earthquakes with different magnitude consistently, we set f_l as proportional to the corner frequency of the event. Using Brune's (1970) model, the corner frequency f_c of an event with moment M_0 is given by $f_c(M_0) = k\beta \left(\frac{16}{7}\Delta\sigma\right)^{1/3} M_0^{-1/3}$, where β is the S-wave velocity (3.3 km/s), $k = 0.37$ (SI unit), and $\Delta\sigma$ is the scaling stress parameter. Fig. 2 shows this relation for three values of $\Delta\sigma$. Because $\Delta\sigma$ typically ranges from 0.3 to 50 MPa (e.g., Allmann & Shearer 2009), we chose the f_l given by this relation for $\Delta\sigma$ =100 MPa. Because of the low-pass filter, our estimate of E_R is band-limited and missing some energy at high frequencies. Thus, we need to correct for the missing energy, as we will discuss in Subsection 2.3.

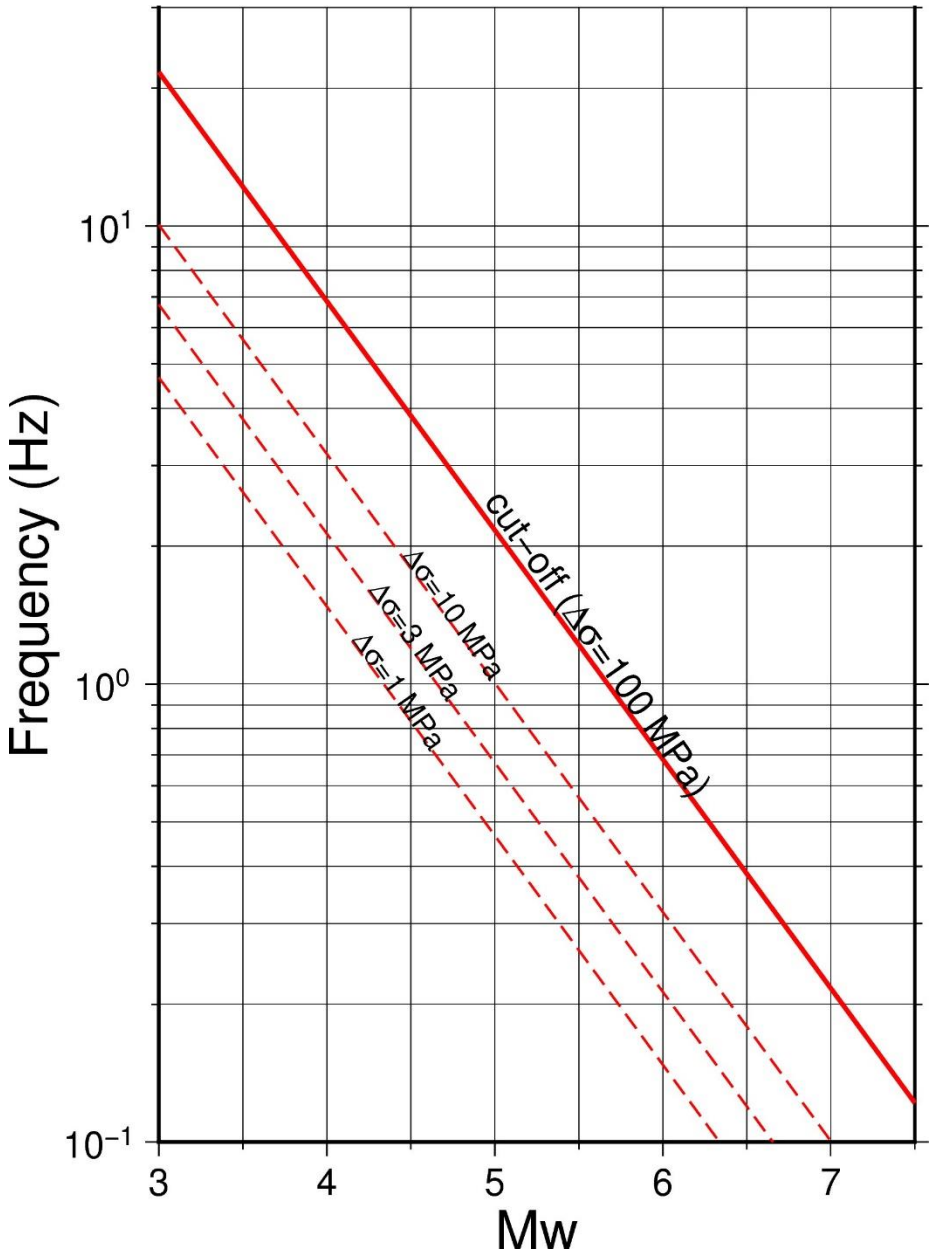

Figure 2. Relationship between the moment magnitude (M_w) and the low-pass cut-off frequency f_l (solid line) and spectral corner frequencies (dashed lines). The dashed lines show the source corner frequencies of the Brune (1970) model for the stress parameters $\Delta\sigma$ of 1 MPa, 3 MPa, and 10 MPa.

Fig. 3 shows five typical examples of the target-event waveform, eGF, and AMRF. We

computed the synthetic waveform of each target event by convolving the AMRF with the eGF. We included the event in our final list only if the synthetic waveform reproduced more than 80% of the power of the observed waveform. Furthermore, even if the derived AMRF met the above condition, we removed it from the final list if it appeared very noisy (about 15% of the total; Text S1).

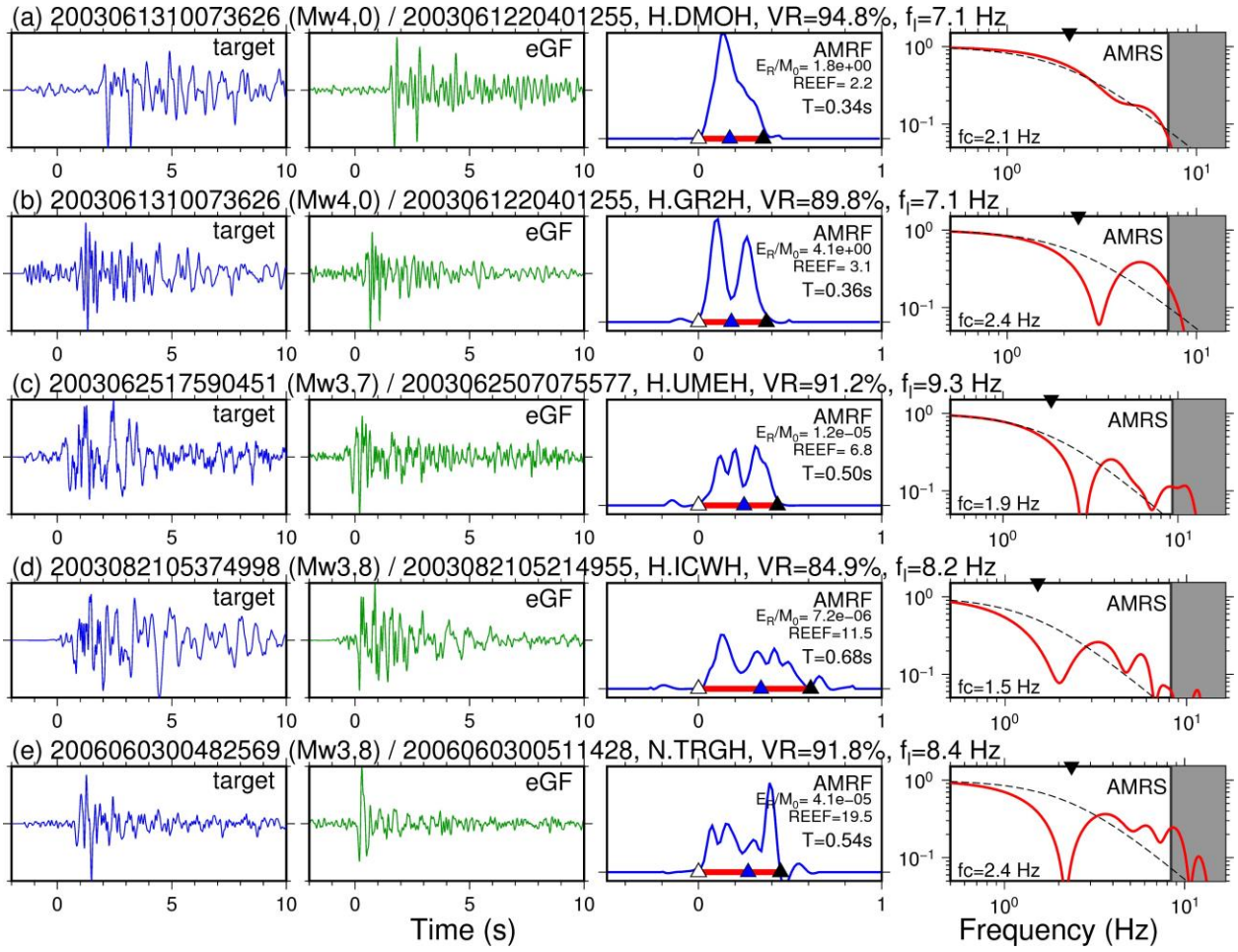

Figure 3. Examples of waveform deconvolution for five earthquakes (a–e). From left to right, the first and second columns show the target seismic waveforms and the eGFs, respectively, and third column shows the AMRF obtained by deconvolution. White, black, and blue triangles show the initiation time t_1, the termination time t_2, and the centroid time t_c, respectively. Red horizontal

lines show the measured duration $T = t_2 - t_1$. The fourth column shows the spectra of the AMRFs. Solid red curves denote the spectra. The black dashed curve shows the best-fit omega-square spectrum, with the black inverted triangle indicating the corner frequency (f_c).

When multiple eGF events were available for one target earthquake, the eGF event that produced AMRFs at the largest number of stations was used. If the number of AMRFs from an eGF event was less than ten, we discarded the AMRFs. We measured the durations of AMRFs by using peak detection (Text S2). We automatically determined the initiation time of the first peak t_1 and the termination time of the last peak t_2, and then calculated the duration by $T = t_2 - t_1$. We cut out the range from $t = t_1 - T/2$ to $t = t_2 + T/2$ of the AMRFs and normalized them so that their time integrals were equal to the seismic moments listed in the F-net catalogue.

Fig. 3a shows a simple triangular AMRF, whereas Figs. 3b–e show examples of AMRFs with multiple pulses, implying complex ruptures at multiple patches. Additionally, we computed the spectra of the AMRFs using the fast Fourier transform (FFT) algorithm. The spectrum of the simple triangular AMRF shows a monotonic decay in amplitude with frequency above a well-defined corner frequency (Fig. 3a). However, the spectra of the complex AMRFs have distinctive troughs (Figs. 3b-e), reflecting the multiple pulses. Because of this complex spectral shape, fitting the spectrum with the commonly-used ω^2-model is difficult, and no clear corner frequency can be defined.

2.3. Estimation of radiated energy and source complexity

The radiated energy, E_R, is estimated by the following (e.g., Vassiliou & Kanamori 1982):

$$E_R = \left(\frac{1}{15\pi\rho\alpha^5} + \frac{1}{10\pi\rho\beta^5}\right) \int M^2(t)dt \qquad (1),$$

where ρ is the density, α is the P-wave velocity, β is the S-wave velocity at the source, and $M(t)$ is the moment-rate function. (In Appendix A, we list the symbols and relationships frequently used in this paper.) We used the medium parameters employed in the F-net moment tensor inversion algorithm (Fig. S1). For $M(t)$, we used the AMRFs obtained in Subsection 2.2. Because the AMRFs were estimated by applying a low-pass filter (Fig. 2), the radiated energy computed with Eq. (1) represents a band-limited value. Hereafter, we refer to this band-limited radiated energy as $\hat{E}_R$.

To estimate the missing high-frequency energy, we assume that the amplitude of the displacement spectrum decays with f^2 for $f > f_l$ in consistency with the ω^2-model (Aki 1967; Brune 1970). In this case, the missing high-frequency energy is calculated as follows:

$$E_R^{\text{missing}} = \frac{4\pi a_l^3 f_l^3}{5\rho\beta^5} \quad (2),$$

where a_l is the spectral amplitude at $f = f_l$. We used the FFT algorithm to compute a_l, and obtained the radiated energy as $E_R = \hat{E}_R + E_R^{\text{missing}}$. Fig. 4a shows the scaled energy ($\hat{E}_R/M_0$), before the correction for missing high-frequency energy. Fig. 4b compares the scaled energy before and after the correction. For earthquakes with a small $\hat{E}_R/M_0$, the effect of the correction is negligible, whereas for earthquakes with a large $\hat{E}_R/M_0$, the correction is large. This is because earthquakes with high scaled energy before the correction have a large amount of high-frequency energy, which is removed by the low-pass filter.

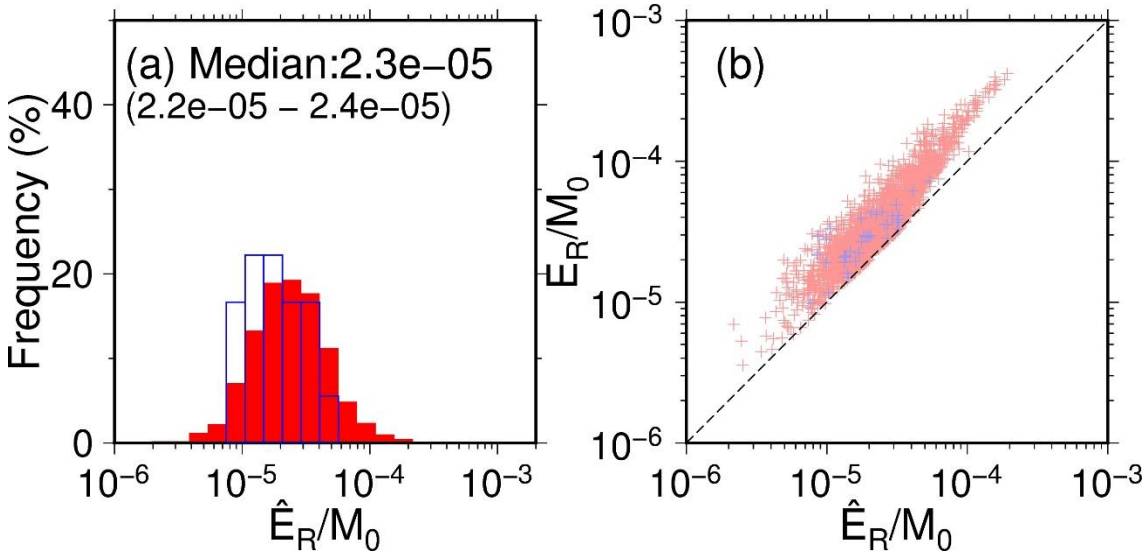

Figure 4. Estimated band-limited scaled energy $\hat{E}_R/M_0$. (a) Frequency distribution of $\hat{E}_R/M_0$. The red colour shows the results from velocity seismograms for M_w<5.5 events, and the blue colour shows the results from strong-motion seismograms for M_w >4.5 events. (b) Comparison of scaled energy before and after the correction for the missing high-frequency energy ($\hat{E}_R/M_0$ and E_R/M_0, respectively).

As a measure of source complexity, we used the radiated energy enhancement factor ($REEF$) proposed by Ye et al. (2018).

$$REEF = \frac{E_{\mathrm{R}}}{E_{\mathrm{Rmin}}} = \frac{5\pi\rho\beta^5}{6}\left(\frac{E_{\mathrm{R}}}{M_0}\right)\left(\frac{T^3}{M_0}\right), \quad (3),$$

where E_{Rmin} is the minimum radiated energy for a given M_0 and source duration T (Kanamori & Rivera 2004). The minimum energy radiation occurs when the moment-rate function is a parabolic (i.e., quadratic) function and $REEF = 1$. As the shape of the moment-rate function becomes more complex, $REEF$ increases. Examples of $REEF$ for some typical moment-rate functions are shown in Fig. S2.

Figs. 5–7 show examples of the azimuthal variation in the AMRF, the scaled energy

197 e_R=E_R/M_0, $REEF$, and M_0/T^3 for 12 events. They show the systematic directional variations
198 caused by rupture propagation. Some earthquakes show simple directivity (Ben-Menahem 1961),
199 where the pulse width and amplitude vary systematically with direction. Fig. 7d shows the 2016
200 M_w=7.0 Kumamoto earthquake, for which the AMRFs are very complex and long in the southwest
201 direction but relatively simple and short in the northeast direction. This directivity is consistent
202 with the previous studies based on different analyses using similar data (Asano & Iwata 2006;
203 Kanamori et al. 2020). Additionally, the directional dependence of the AMRFs of the 2017 Akita-
204 Daisen earthquake (Fig. 7b) is consistent with that in previous study using a similar method
205 (Yoshida et al. 2020). We selected the station with the median radiated energy for each event and
206 used that AMRF as representative of the event. The representative values of E_R, $REEF$, and T for
207 that event were calculated from the representative AMRF.
208

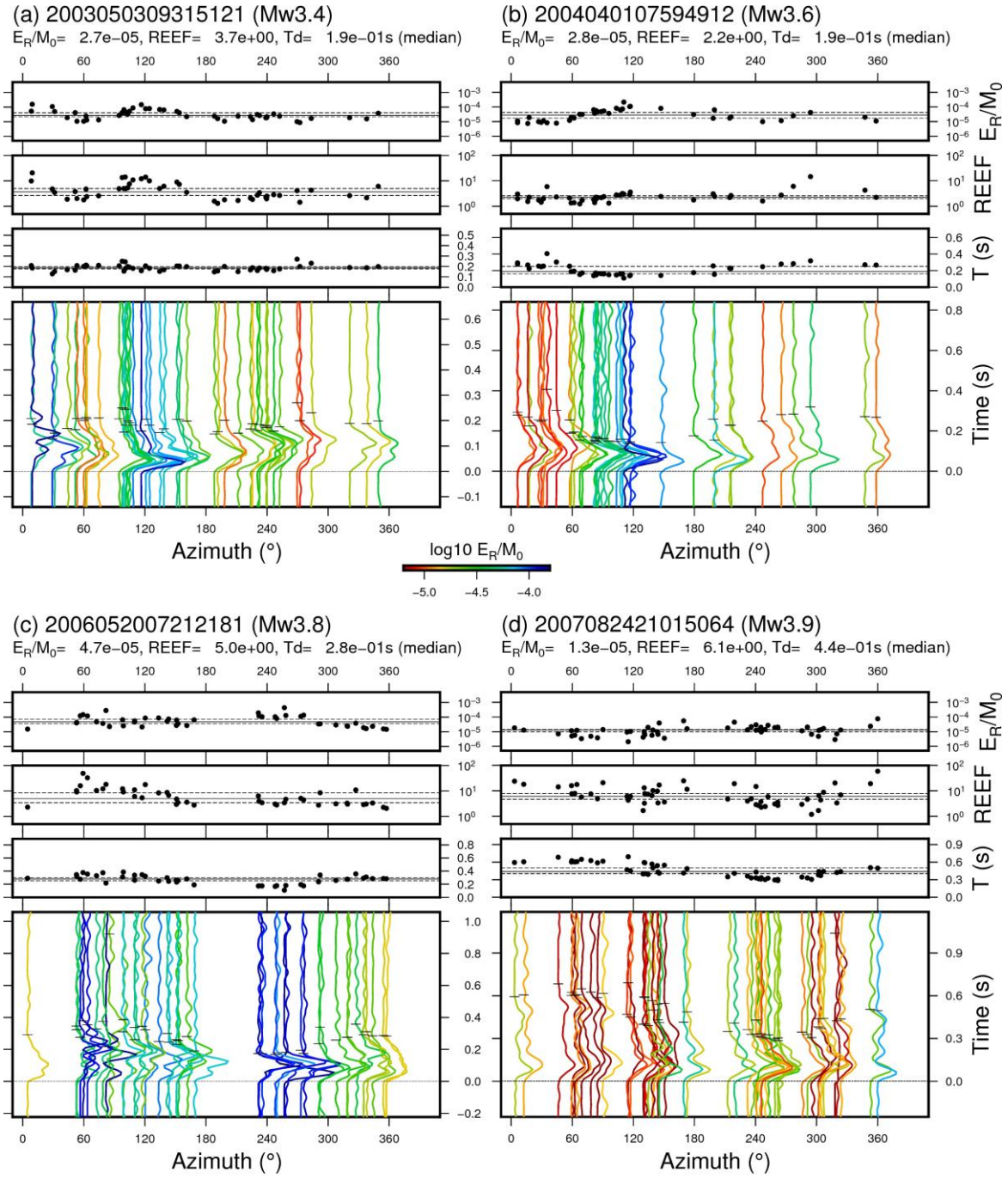

209

210 **Figure 5.** Examples of directional dependence in AMRFs, $e_R = E_R/M_0$, $REEF$, and M_0/T^3 for four
211 earthquakes of (a) M_w 3.4, (b) M_w 3.6, (c) M_w 3.8, and (d) M_w 3.9. The horizontal lines in the upper
212 three diagrams in each panel represent the median values of e_R, $REEF$, and M_0/T^3. The horizontal
213 dashed line represents the 95% confidence interval.

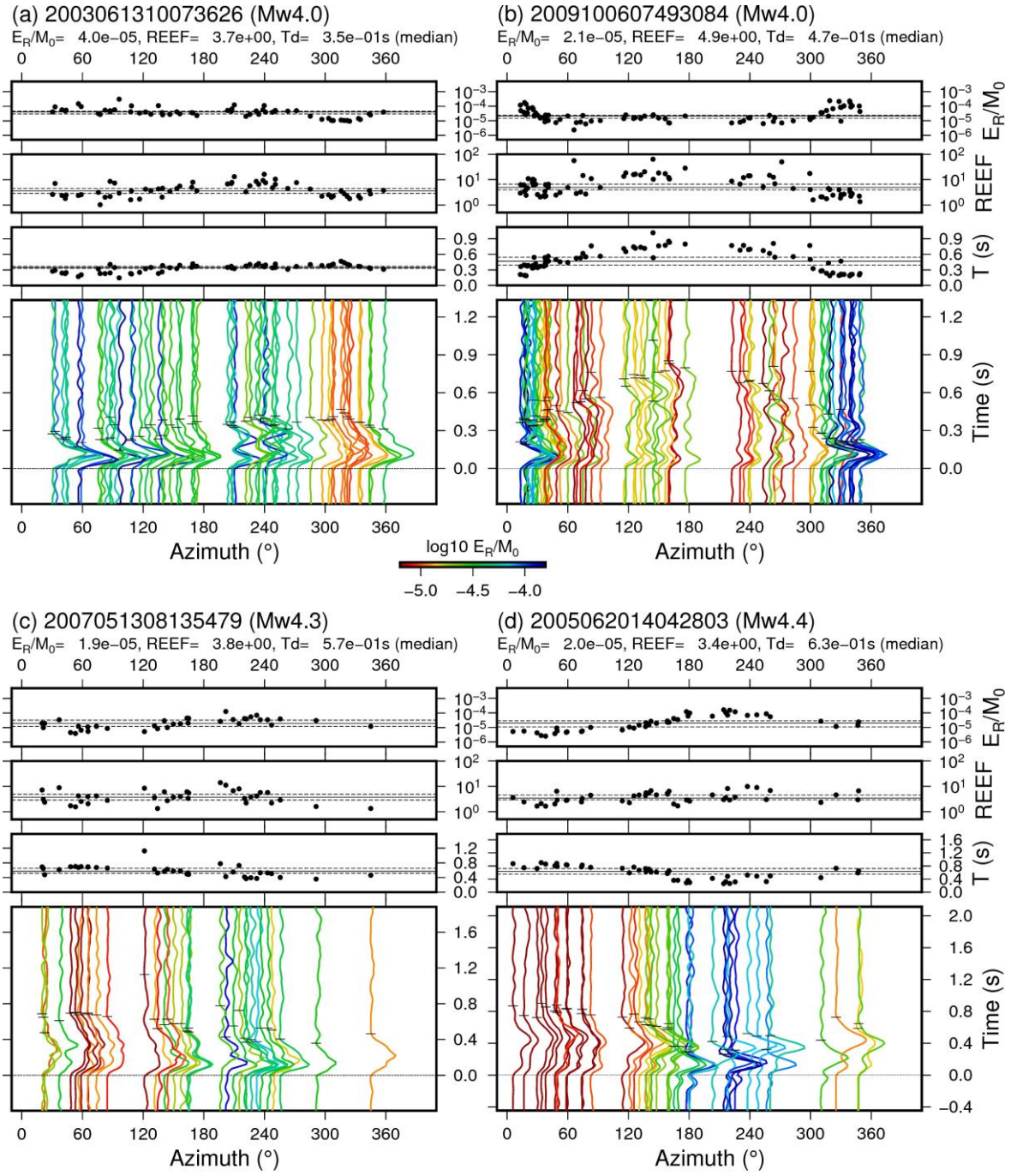

214

215 **Figure 6.** Examples of directional dependence in AMRFs, $e_R = E_R/M_0$, $REEF$, and M_0/T^3 for four

216 earthquakes of (a) M_w 4.0, (b) M_w 4.0, (c) M_w 4.3, and (d) M_w 4.4. The horizontal lines in the upper

217 three diagrams in each panel represent the median values of e_R, $REEF$, and M_0/T^3. The horizontal

218 dashed line represents the 95% confidence interval.

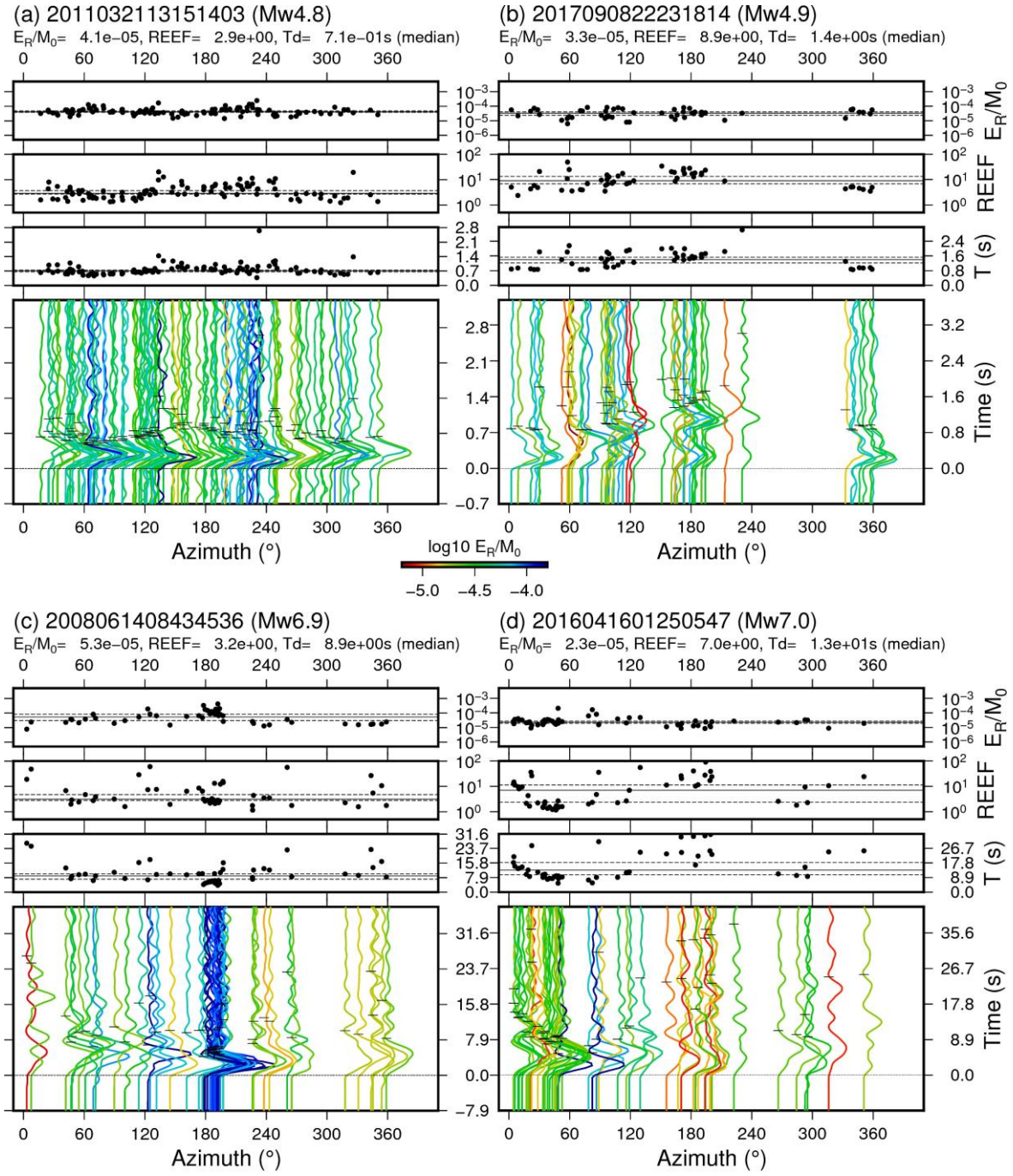

Figure 7. Examples of directional dependence in AMRFs, $e_R = E_R/M_0$, $REEF$, and M_0/T^3 for four earthquakes of (a) M_w 4.8, (b) M_w 4.9, (c) M_w 6.9, and (d) M_w 7.0. The horizontal lines in the upper three diagrams in each panel represent the median values of e_R, $REEF$, and M_0/T^3. The horizontal dashed line represents the 95% confidence interval.

There were 5445 cases where the AMRFs were obtained with more than ten different eGF events for the same earthquake-station pair. To see the stability of these results, we calculated the median (Med) and median absolute deviation (MAD) of the results obtained by using the different eGF events for each pair (Figs. S3a–c). We then computed $\mathrm{rMAD} = \mathrm{MAD}/\mathrm{Med}$ as a rough indicator of the percentage spread of the T, e_R, and $REEF$ estimates. The distributions of rMAD are shown in Figs. S3d–f. The medians rMAD values were 0.11, 0.27, and 0.25 for T, e_R, and $REEF$, respectively.

3. Results

We estimated the scaled energy $e_R = E_R/M_0$, $REEF$, and duration T for 1736 earthquakes. Of these, 1700 were of $M_w < 5.5$, for which we used velocity waveforms, and 36 were of $M_w \geq 4.5$, for which we used acceleration waveforms.

3.1. Radiated energy

The frequency distributions of the scaled energy $e_R = E_R/M_0$, $REEF$ after the correction, and M_0/T^3 are shown in Fig. 8a–c. The correction (Fig. 4b) increased the median of the scaled energy from 2.4×10^{-5} to 3.7×10^{-5}. For each event, we computed the 95% confidence intervals of the median values of e_R and $REEF$ using 1000 different combinations of stations based on bootstrap re-samplings. We calculated $e_R^{err} = e_R^{max}/e_R^{min}$ and $REEF^{err} = REEF^{max}/REEF^{min}$ to express the uncertainty of the estimated results, where the superscripts max and min represent the upper and lower limits, respectively. The frequency distribution of e_R^{err} and $REEF^{err}$ is shown in Fig. S4; the median e_R^{err} is 2.0 and the median $REEF^{err}$ is 1.8. However, the overall diversity of e_R and $REEF$ among different earthquakes varied approximately several- to ten-fold (Figs. 8a-b), significantly larger than the estimation uncertainties for individual results.

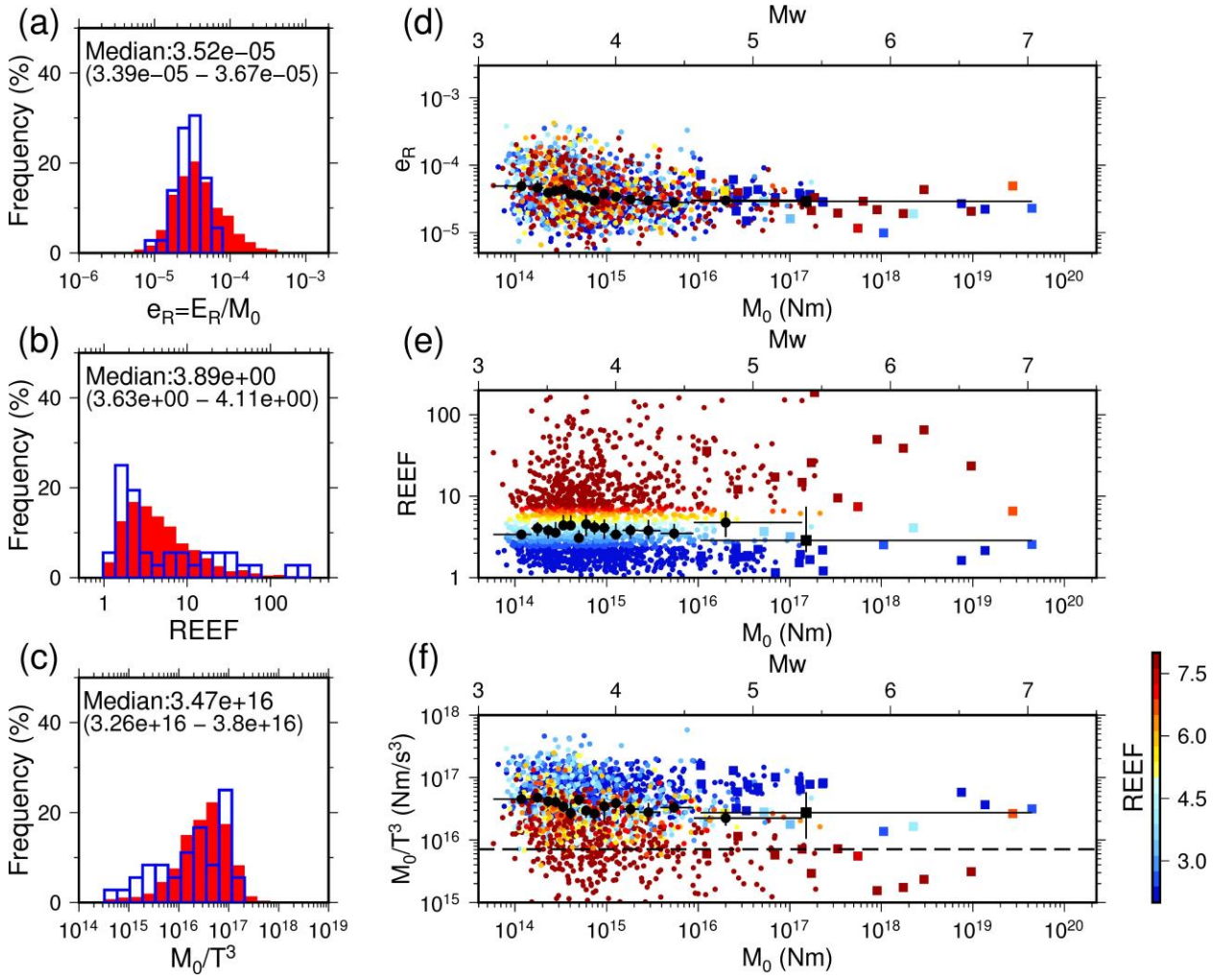

Figure 8. Estimated scaled energy $e_R = E_R/M_0$, $REEF$, and M_0/T^3. (a)-(c) Frequency distributions for the three variables, respectively. Red colour shows the results from velocity seismograms for Mw<5.5 events, while blue shows the results from acceleration seismograms for Mw>4.5 events. The numbers in parentheses indicate the 95% confidence interval of the median. Dependence of (d) e_R, (e) $REEF$, and (f) M_0/T^3 on the seismic moment M_0. Circles show the results from velocity seismograms, while squares show the results from acceleration seismograms. $REEF$ is shown according to the colour scale given in the figure. Large black symbols show the median values, and the horizontal line denotes the range of the data used. Vertical lines indicate the 95% confidence interval of the median values. The dashed horizontal line in (f) shows the global M_0/T^3

trend (Duputel et al. 2013).

The present results include 13 earthquakes in common with Kanamori et al. (2020) in which E_R is estimated with a very different method. Table 1 compares the E_R values in this study with the E_{R_final} in Kanamori et al. (2020). For 12 events, the difference is within a factor of three. Even for the remaining one event, the difference is approximately a factor of four. Moreover, the results of this study are in good agreement with those of other studies using the empirical Green's function method, as shown in Table 1.

Table 1. Comparison with results from Kanamori et al. (2020) and other studies. (1) Izutani (2005), (2) Izutani (2008), (3) Baltay et al. (2011), and (4) Ross et al. (2018).

Event	JMA ID	M_w (F-net)	E_R This study	E_R_final Kanamori et al. (2020)	E_R Other studies
2004 Chuetsu	2004102317560030	6.52	2.11 E+14 J	3.92 E+14 J	3.2 E+14 J (1) 2.9 E+14 J (3)
2004 Chuetsu aftershock	2004102318340569	6.24	1.44 E+14 J	6.76 E+13 J	
2007 Noto	2007032509415791	6.69	3.12 E+14 J	8.69 E+14 J	6.8 E+14 J (2)
2008 Iwate-Miyagi	2008061408434536	6.89	1.44 E+15 J	7.91 E+14 J	1.8 E+15 J (3)
2011 Ibaraki	2011031918564806	5.80	1.95 E+13 J	1.50 E+13 J	
2011 Fukushima	2011041117161202	6.59	2.04 E+14 J	4.95 E+14 J	
2013 Tochigi	2013022516235358	5.76	6.46 E+13 J	1.69 E+13 J	
2016 Kumamoto foreshock	2016041421263443	6.10	3.40 E+12 J	5.12 E+12 J	
2016 Kumamoto foreshock	2016041500034645	5.95	1.33 E+13 J	3.34 E+13 J	

2016 Kumamoto	2016041601250547	7.03	1.03 E+15 J	2.09 E+15 J	
2016 Tottori	2016102114072257	6.17	4.51 E+13 J	4.95 E+13 J	5.8 E+13 J [4]
2016 Ibaraki	2016122821384904	5.90	2.03 E+13 J	9.85 E+12 J	
2018 Shimane	2018040901323081	5.62	6.65 E+12 J	4.91 E+12 J	
2018 Osaka	2018061807583414	5.51	8.72 E+12 J	1.12 E+13 J	

3.2. Absolute value and scale dependence of the scaled energy, $REEF$, and M_0/T^3

The median values of the scaled energy $e_R=E_R/M_0$, $REEF$, and M_0/T^3 were 3.7×10^{-5}, 3.8, and 3.5×10^{16}, respectively. We found no clear difference between the estimates for the M_w<5.5 earthquakes using velocity waveform data and those for the M_w≥4.5 earthquakes using acceleration waveform data.

Fig. 8d–f compares the scaled energy $e_R = E_R/M_0$, $REEF$, and M_0/T^3 with M_0. E_R increases with M_0 (Fig. S5); nevertheless, no strong correlations were found between e_R and M_0 for M_w 3–7 (Fig. 8d). However, the e_R for smaller earthquakes (M_w<4) appears to have a weak, decreasing trend with M_0. Similarly, the median M_0/T^3 decreases slightly as M_w increases from 3 to 4 (Fig. 8f). No such trends are evident for earthquakes with M_w 4–7. Hence, the weak decreasing trends for M_w<4 events may be related to low signal-to-noise ratios of the eGFs for smaller earthquakes. The median values of $REEF$ do not show a significant dependence on M_0 (Fig. 8e).

The apparent stress $\sigma_a = \mu\left(E_R / M_0\right)$ (Wyss & Brune 1968; Wyss 1970) is a useful stress parameter that can be related to energy radiation. Because the static stress drop $\Delta\sigma$ is subject to large uncertainties, the scaled energy $e_R=E_R/M_0$ or σ_a are alternative stress parameters for studying the difference in earthquake source characteristics (Kanamori et al. 1993; Kanamori & Heaton 2000; Kanamori & Rivera 2006). However, comparing the scaled energies of earthquakes with different magnitudes is challenging because the comparison requires a wide range of

frequencies, and the scale dependence remains under debate. Some previous studies showed that scaled energy or apparent stress increases with earthquake size (e.g., Abercrombie 1995; Mayeda & Walter 1996; Jost et al. 1998; Izutani & Kanamori 2001; Prejean & Ellsworth 2001; Mori et al. 2003; Izutani 2005, 2008; Takahashi et al. 2005; Mayeda et al. 2005; Malagnini et al. 2008; Malagnini et al. 2014; Nishitsuji & Mori 2014), whereas others suggested that the scaled energy is independent of earthquake size (e.g., Ide & Beroza 2001; Pérez-Campos & Beroza 2001; Baltay et al. 2010; Baltay et al. 2011; Baltay et al. 2014; Zollo et al. 2014; Denolle & Shearer 2016; Ye et al. 2016a; Chounet et al. 2018). The e_R in our dataset does not show a strong size dependence from M_w 3–7.

The scaled energy e_R obtained in this study varied from 5×10^{-6} to 4×10^{-4} (Fig. 8a). This range is much narrower than the range of 10^{-7} to 10^{-3} obtained in previous studies (Vasiliou & Kanamori 1982; Singh & Ordaz 1994; Abercrombie 1995; Newman & Okal 1998; Ide & Beroza 2001; Kanamori & Rivera 2004; Venkataraman & Kanamori 2004; Jin & Fukuyama 2005; Choy et al. 2006; Convers & Newman 2011; Baltay et al. 2014; Kanamori et al. 2020). The value of e_R varies among tectonic environments (Choy & Boatwright 1995; Newman & Okal 1998; Venkataraman & Kanamori 2004; Ji & Fukuyama 2005; Ye et al. 2013; Ye et al. 2016b; Kanamori & Ross 2019). Crustal earthquakes often have a larger e_R than interplate earthquakes (Venkataraman & Kanamori 2004). Venkataraman & Kanamori (2004) estimated the e_R of six M_w>6.7 crustal earthquakes at 2×10^{-5} to 3×10^{-4}. Kanamori et al. (2020) estimated the e_R of 29 M_w>5.5 crustal earthquakes in Japan at 6×10^{-6} to 1×10^{-4}. These ranges are comparable to the results of this study.

The median $REEF$ obtained in this study was 3.8, with individual values ranging from 2 to 30. Ye et al. (2018) estimated the $REEF$ of M_w>7 interplate earthquakes, and found a range of 10 to 100, which is larger than the present results. $REEF$ is proportional to T^3 (where T is duration,

313 Eq. 3); therefore, this difference could result from differences in the way T was measured. The
314 median M_0/T^3 obtained in this study for M_w 3–7 earthquakes was 3.5×10^{16}, which was
315 approximately five times larger than that of the global M_w>6.5 events, at 7.1×10^{15}, as estimated
316 from the centroid time delay (Duputel et al. 2013) (Fig. 8f). Thus, given the differences in the
317 definition of T, we consider that the relative, rather than absolute, variation in $REEF$ in the
318 individual data is relevant. Our results (Fig. 8e) show that $REEF$ has no obvious size dependence
319 at M_w 3–7.
320
321 **3.3. Dependence on the depth and the faulting style**
322 Fig. 9 compares the depth with e_R, $REEF$, and M_0/T^3. Although few events deeper than 15
323 km were examined, no significant variation with depth is discernible. Our finding that e_R does not
324 strongly depend on depth is consistent with the globally compiled results (Bilek et al. 2004;
325 Venkataraman & Kanamori 2004; Ye et al. 2016b, Denolle & Shearer 2016), except for shallow
326 tsunami earthquakes.
327

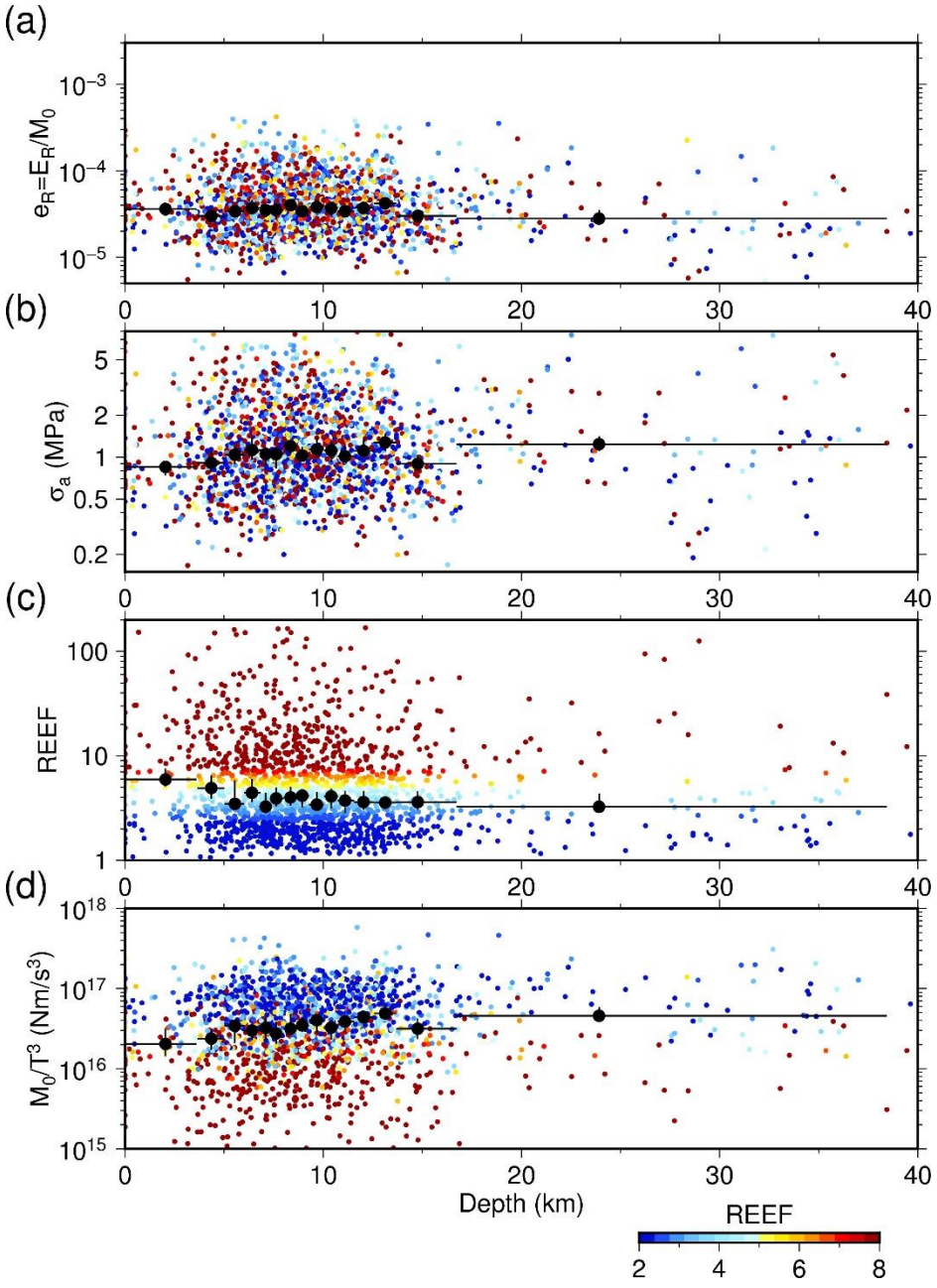

328

329 **Figure 9.** Dependence of (a) scaled energy $e_R = E_R/M_0$, (b) apparent stress, (c) $REEF$, and (d)

330 M_0/T^3 on depth. $REEF$ is shown according to the colour scale in the figure. Large black circles

331 show the median values, and the horizontal line denotes the range of the data. Vertical lines indicate

332 the 95% confidence interval of the median values.

333

Some controversy has arisen over the dependence of e_R on the focal mechanism type (Choy & Boatwright 1995; Newman & Okal 1998; Pérez-Campos & Beroza 2001). In particular, some studies reported that e_R is systematically larger for strike-slip fault earthquakes (Choy & Boatwright 1995; Pérez-Campos & Beroza 2001; Choy & Kirby 2004; Choy et al. 2006; Convers & Newman 2011; Batlay et al. 2014); however, others found no significant differences (Abercrombie 1995; Mayeda & Walter 1996; Newman & Okal 2004; Kanamori & Ross 2019; Kanamori et al. 2020). Others have suggested that the difficulty of correcting the radiation pattern may have caused the apparent variations (Newman & Okal 1998).

Fig. 10 compares e_R, $REEF$, and M_0/T^3 with the type of faulting. We classified the focal mechanisms listed in the F-net catalogue by the scalar parameter $C_\mathrm{m} = \frac{\phi}{|\phi|}\frac{180-|\phi|}{90}$ according to Shearer et al. (2006). Here, ϕ is the rake angle (ranging from -180° to 180°) of the nodal plane with the smaller absolute value of rake angle. C_m is related to the slip direction and ranges from -1 to 1, taking the value of -1 for pure normal-fault motion, 0 for pure strike-slip-fault motion, and 1 for pure reverse-fault motion. We found no obvious dependence of e_R, $REEF$, and M_0/T^3 on faulting type.

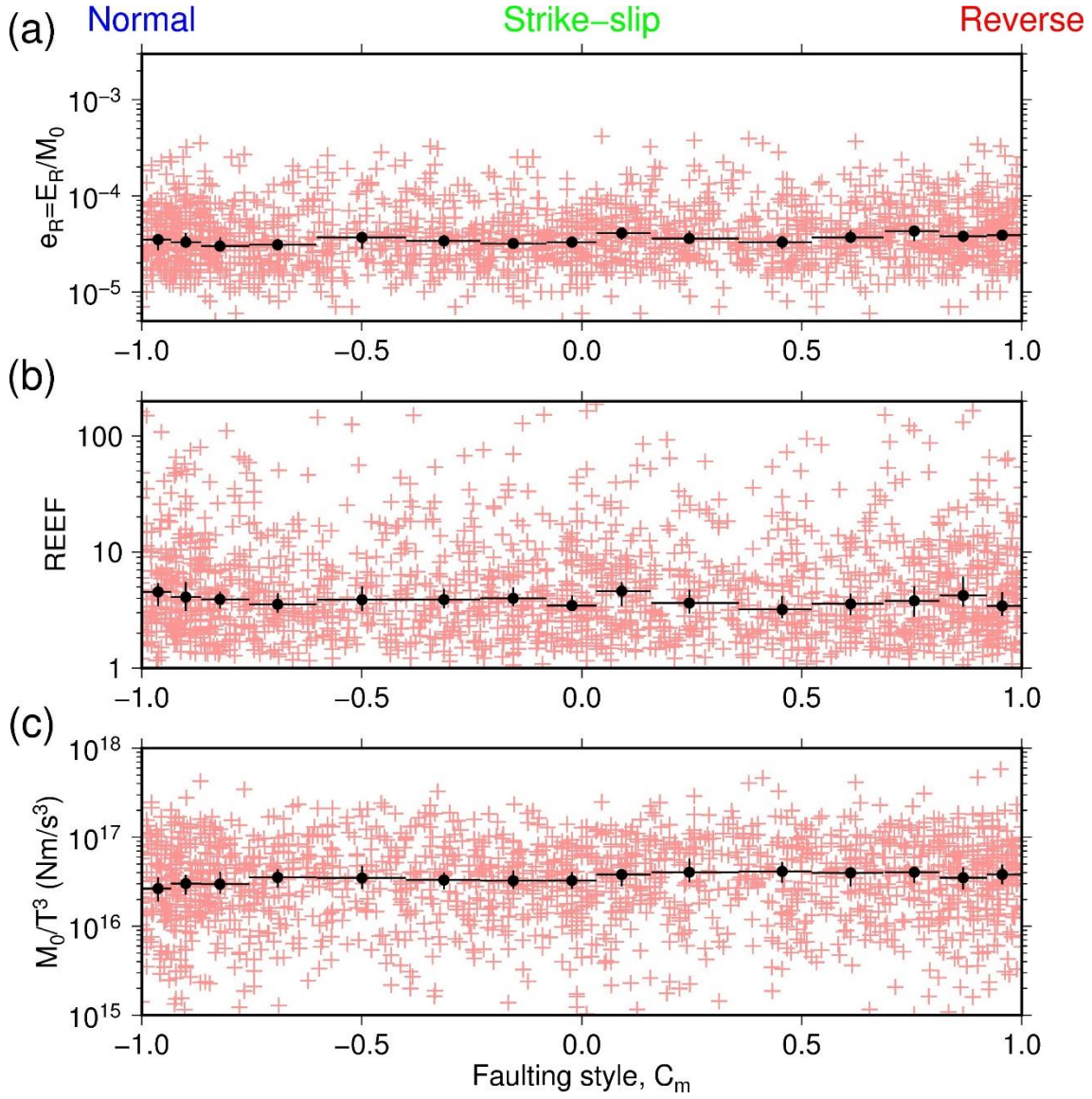

Figure 10. Dependence of scaled energy $e_R = E_R/M_0$, $REEF$, and M_0/T^3 on faulting style. Black circles show the median values, with the horizontal line denoting the data range. Vertical lines indicate the 95% confidence interval of the median values.

4. Discussion

4.1. Relation between source duration *T* and corner frequency *fc*

In our time-domain analysis, we used the duration, T, rather than the commonly used corner

358 frequency, f_c, to define the temporal scale of the events. To clarify the relationship between T and
359 f_c, we compared them for the events used in this study. We measured the corner frequencies in the
360 frequency domain using the standard procedure based on the ω^2-model. We first computed the
361 spectrum of each AMRF using the FFT method. We did not smooth the spectra, because smoothing
362 may distort the spectral shape. Fig. 11 shows the spectra of AMRFs at each station of the M_w=4.0
363 event shown in Fig. 6a. The low-frequency level is normalized at 1. Other examples are shown in
364 Figs. S6-9. The spectra of the AMRFs with high $REEF$ tend to have complex spectral shapes,
365 significantly different from their ω^2-spectrum (azimuth from 180° to 300°).

366

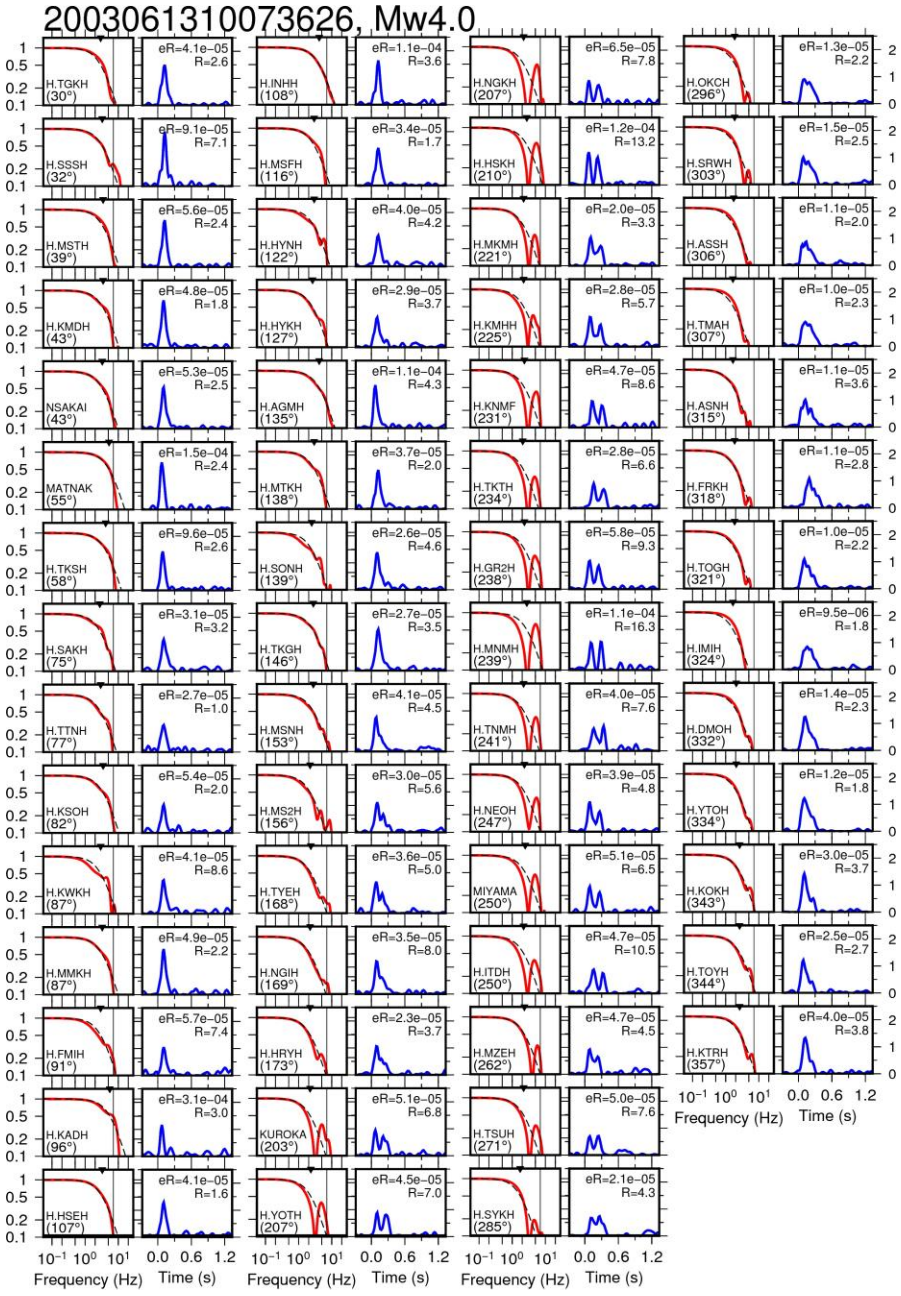

367

368 **Figure 11.** Examples of AMRF spectra for an $M_w = 4.0$ event. The corresponding AMRFs are
369 shown in Fig. 6a. The red curves on the left side of each panel show the AMRF spectra. The black
370 dashed curves show the best-fit omega-square spectra, and the black inverted triangles indicate the
371 corner frequency, f_c. The vertical line represents the cut-off frequency. The number in parentheses
372 indicates the azimuths of the respective seismic station. The blue curve on the right side of each
373 panel shows the AMRF.

We fit the spectrum of all the events to the ω^2–spectrum and minimized the variance using

$$J = \sum_{k=1}^{n_{freq}} \left\{ \log\left(A(f_k)\right) - \log\left(\frac{1}{1+(f_k/f_c)^2}\right) \right\}^2 \quad (4),$$

where n_{freq} is the number of frequency points, f_k is the frequency point ($f_k < f_l$), and $A(f)$ is the normalized AMRF spectal amplitude. The corner frequency, f_c, is determined by minimizing J. In equation (4), both the frequency and the amplitude are sampled at equal intervals on a logarithmic scale (this sampling scheme is denoted by loglog in this paper). Fig. 12a shows the variance as a function of $REEF$; it is minimized at $REEF \approx 3$. This result can be interpreted as follows. The moment-rate function that has the ω^2-spectrum is given by $t \exp(-2\pi f_c t)$ (t: time) (Brune 1970). This function reaches a maximum at $t = t_p = 1/2\pi f_c$. Although the duration of this function is not finite, at $t = 5t_p$ it decreases to less than 10 % of the maximum; hence, we define the duration by $T = 5/2\pi f_c$. In our time-domain analysis, we measured the duration of the observed AMRF with approximately 10 % amplitude threshold. Fig. S2c shows that $REEF$ is approximately 3 for this truncated AMRF function. Thus, Fig. 12a indicates that, if the AMRF is a simple pulse-like function with $REEF \approx 3$, then the ω^2-model is a good model; additionally, T and f_c can be directly related by $T = 5/2\pi f_c$. For complex AMRFs with large $REEF$s, simple relationship does not exist between T and $1/f_c$. Figs. 12b and c show the relationships we obtained for our data set. Although we used the loglog sampling scheme above, we can similarly define "linlin", "linlog" and "loglin" sampling schemes and show the same trend (Fig. S10).

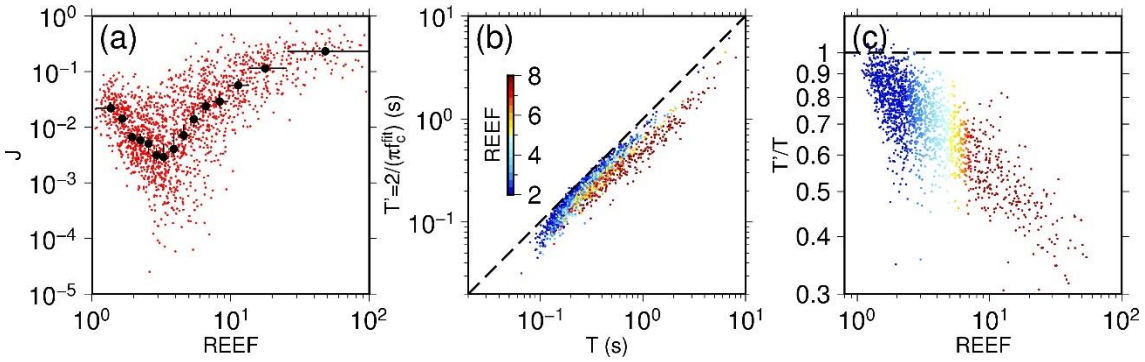

Figure 12. Relationships with corner frequency estimated using spectral fitting and duration. (a) Relationship between $REEF$ and the residual of spectral fitting J. (b) Comparison of the durations measured in the time domain (T) and those in the frequency domain (T') from the corner frequency. T' was calculated assuming the triangular moment-rate function (Eq. A2). $REEF$ is shown according to the colour scale. (c) Comparison of REEF and T'/T.

4.2. Comparison of the results with time-domain and frequency-domain methods

In the time-domain method, we have three independent parameters, M_0, E_R, and T. To compare our time-domain results with the frequency domain results, Fig. 13 shows the relationship given by equation (3), using 2 non-dimensional parameters $e_R = \frac{E_R}{M_0}$ and $\left(\frac{M_0}{\mu\beta^3 T^3}\right)$ with $REEF$ as a parameter. For the ω^2-model, $REEF \approx 3$ as shown above. The black solid line on Fig. 13 shows the relationship for the ω^2-model where $T = 5/2\pi f_c$ is used.

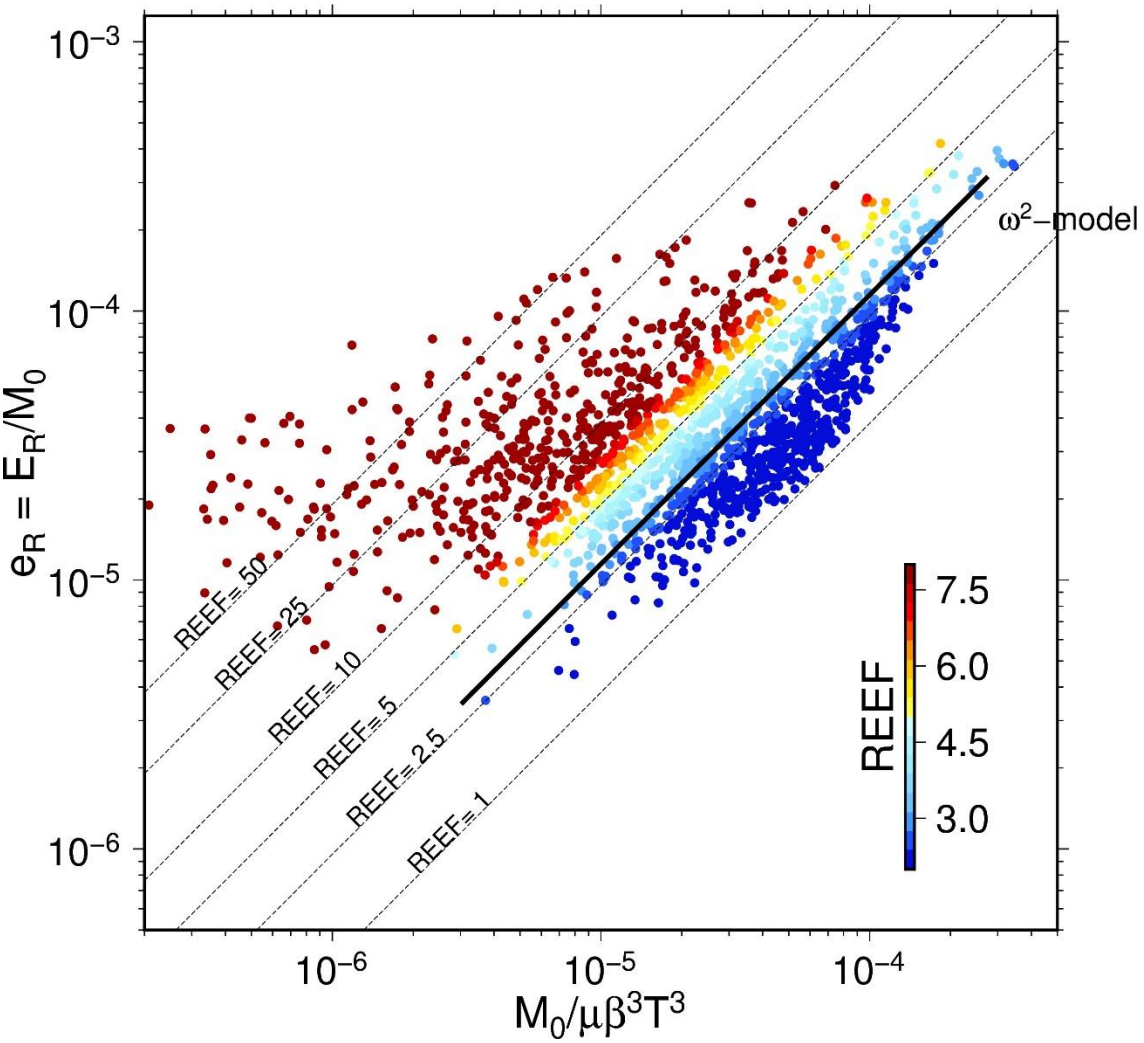

408

409 **Figure 13.** The relationship between $e_R = E_R/M_0$, $REEF$, and $M_0/\mu\beta^3T^3$. $REEF$ is shown

410 according to the colour scale. The thick black line shows the relationship for the ω^2-model

411 (Brune 1970).

412

413 About 60% of our events (in blue) closely follow this line. Thus, if the events are

414 relatively simple with a small $REEF$ (< 5), our results are consistent with those for the ω^2-model.

415 However, the results for events with a large $REEF$ deviate significantly from this trend, as shown

416 in Fig. 13.

417 Note that there is no parameter in the ω^2-model that directly measures the spatial length

in the model (e.g., radius a of a circular fault). The corner frequency f_c is a kinematic parameter determined from the wave-field. Thus, in principle, the static stress drop, $\Delta\sigma$, cannot be determined from this type of analysis. Brune (1970) linked the ω^2-model to a circular crack model with a radius a using a simple relationship ($f_c = c\beta / 2\pi a$, where c=2.34), which is based on qualitative energy partitioning and is somewhat heuristic, but it is a reasonable relation for relatively smooth ruptures, because if $T = 5/2\pi f_c$, the corresponding rupture speed, a/T, is a significant fraction of the shear-wave speed, 0.468β. With this relationship, we can relate f_c to the static stress drop $\Delta\sigma$ of a circular fault using Eshelby's (1957) relation as follows:

$$\Delta\sigma = \left(\frac{7\pi^3}{2c^3}\right)\mu\left(\frac{M_0 f_c^3}{\mu\beta^3}\right) = \left(\frac{875}{16c^3}\right)\mu\left(\frac{M_0}{\mu\beta^3 T^3}\right). \qquad (5)\ .$$

However, because no directly measured spatial parameter is used, this should be regarded as an approximate stress drop inferred from f_c, which may be more appropriately called a stress parameter (Boore 1983; Atkinson & Beresnev 1997). Nevertheless, for a smooth simple rupture, it is a conceptually useful measure of the static stress drop.

For the ω^2-model, the radiated energy E_R is given by $E_R = \frac{\pi^2}{5\mu\beta^3} M_0^2 f_c^3$. Using this equation and equation (5), the radiation efficiency (the ratio of E_R to the total static energy released by a fault if the stress drop is from $\Delta\sigma$ to 0) for this model is given by the following:

$$\eta_R = 2\left(\frac{\mu}{\Delta\sigma}\right)\left(\frac{E_R}{M_0}\right) = \frac{4c^3}{35\pi} \qquad (6).$$

For Brune's (1970) model, c is fixed at 2.34, and $\eta_R = 0.47$ regardless of $\Delta\sigma$ (e.g., Madariaga &

436 Ruiz 2016). Note that only if a circular fault with $c = 2.34$ is used, $\Delta\sigma$ can be determined and η_R
437 $= 0.47$. The radiation efficiency $\eta_R = 0.47$ appears to be a reasonable rough average for ordinary
438 brittle events in the crust, but it may vary considerably among individual events.

439

440 **4.3. Earthquakes with large REEF**

441 The large $REEF$ events, such as those shown in Fig. 3b–e, significantly deviate from the trend of
442 the ω^2-model shown in Fig. 13. No obvious way exists to relate T to the spatial scale for complex
443 events; hence, $\Delta\sigma$ and η_R cannot be determined for these events. However, despite its ambiguity,
444 because $\Delta\sigma$ is a stress parameter widely used in seismology, here we attempt to relate our results
445 to the $\Delta\sigma$ and η_R obtained with the ω^2-model.

446 From the definition of η_R, we can write η_R as

447 $$\eta_R = \frac{2\mu}{\Delta\sigma}\left(\frac{E_{R\min}}{M_0}\right)REEF \qquad (7)$$

448 in terms of $REEF$. Then, for an event with $REEF = R$ and duration T, $\Delta\sigma$ can be written as

449 $$\Delta\sigma = \left(\frac{\eta_{R\_\omega}}{\eta_R}\right)\left(\frac{R}{R_\omega}\right)\Delta\sigma_\omega \qquad (8),$$

450 where the subscript ω indicates the parameters for the ω^2-model with the same event duration T.
451 In the above, $R_\omega = 3$ for the ω^2-model. This relation can be regarded as an extension of the
452 widely used method for estimating $\Delta\sigma$ from seismic observations.

453 Because equation (6) involves both $REEF$ and η_R, $\Delta\sigma$ cannot be uniquely related to

454 $\Delta\sigma_\omega$; nevertheless, it can be used to explore the range of $\Delta\sigma$ for various situations. For example,
455 if we assume that simple and complex events in similar tectonic environments have
456 approximately the same average η_R, then $\Delta\sigma = (R / R_\omega)\Delta\sigma_\omega$. If R =15, then $\Delta\sigma$ is 5 times larger
457 than that for the ω^2-model. It has been shown that the stress drop can be considerably larger for a
458 complex rupture (e.g., Rudnicki & Kanamori 1981; Das 1988), although exactly how large
459 depends on the rupture characteristics. Thus, this result is qualitatively consistent with larger $\Delta\sigma$
460 values for events with a larger $REEF$.
461
462 **5. Conclusion**
463 We systematically estimated the radiated energy, E_R, and the source complexity of M_w 3–7
464 earthquakes in the island crust of Japan using a time-domain analysis method. We first created a
465 large database of apparent moment-rate function (AMRF) for 1,736 events using high-quality
466 seismic network data from Japan. We estimated the E_R and the source duration, T from the AMRFs
467 and used them to quantify the source complexity using the radiated energy enhancement factor
468 ($REEF$; Ye et al. 2018). The e_R ranged from 5×10^{-6} to 4×10^{-4} with a median of 3.7×10^{-5}, and $REEF$
469 ranged from 1 to 200 with a median of 3.8. The e_R and $REEF$ did not strongly depend on the
470 seismic moment for M_w 3–7; moreover, e_R and $REEF$ did not depend on the focal mechanism or
471 the event depth. Therefore, the ruptures of small earthquakes have a similar degree of complexity
472 to those of large earthquakes at their representative spatial scales.
473 Approximately one third of the total events had complex AMRFs that were distinct from a
474 single-pulse AMRF. For simple events, the time-domain and the frequency-domain methods
475 yielded similar source parameter results. However, the spectral shape of complex events deviated
476 from the ω^2-model; thus, the significance of the corner frequency was ambiguous. In our time-

477 domain method, the use of T, determined with empirical Green's functions, allows for
478 determination of a more detailed energy release pattern. Moreover, through the use of the
479 complexity parameter, $REEF$, we can systemically present the scaling relation between e_R and T
480 in a systematic way.
481
482
483 **Acknowledgments**
484 We would like to thank Hisahiko Kubo for providing information about machine-learning
485 algorithms. The figures were created using GMT (Wessel and Smith 1998). This research was
486 supported by JSPS KAKENHI (Grant Numbers JP 20K14569).
487

References

Abercrombie, R.E. (2021) Resolution and uncertainties in estimates of earthquake stress drop and energy release. *Philos. Trans. R. Soc. A Math. Phys. Eng. Sci.*, **379**, 20200131, The Royal Society Publishing. doi:10.1098/rsta.2020.0131

Abercrombie, R.E. (1995) Earthquake source scaling relationships from -1 to 5 ML using seismograms recorded at 2.5-km depth. *J. Geophys. Res.*, **100**, 24015–24036, Wiley Online Library. doi:10.1029/95jb02397

Aki, K. (1967) Scaling law of seismic spectrum. *J. Geophys. Res.*, **72**, 1217–1231. doi:10.1029/JZ072i004p01217

Allmann, B.P. & Shearer, P.M. (2009) Global variations of stress drop for moderate to large earthquakes. *J. Geophys. Res. Solid Earth*, **114**. doi:10.1029/2008JB005821

Asano, K. & Iwata, T. (2016) Source rupture processes of the foreshock and mainshock in the 2016 Kumamoto earthquake sequence estimated from the kinematic waveform inversion of strong motion data 2016 Kumamoto earthquake sequence and its impact on earthquake science and hazard assess. *Earth, Planets Sp.*, **68**, 1–11, SpringerOpen. doi:10.1186/s40623-016-0519-9

Atkinson, G.M. & Beresnev, I. (1997) Don't Call it Stress Drop. *Seismol. Res. Lett.*, **68**, 3–4. doi:10.1785/gssrl.68.1.3

506 Baltay, A., Prieto, G. & Beroza, G.C. (2010) Radiated seismic energy from coda measurements
507 and no scaling in apparent stress with seismic moment. *J. Geophys. Res. Solid Earth*, **115**.
508 doi:10.1029/2009jb006736

509 Baltay, A., Ide, S., Prieto, G. & Beroza, G. (2011) Variability in earthquake stress drop and
510 apparent stress. *Geophys. Res. Lett.*, **38**, Wiley Online Library. doi:10.1029/2011GL046698

511 Baltay, A.S., Beroza, G.C. & Ide, S. (2014) Radiated Energy of Great Earthquakes from
512 Teleseismic Empirical Green's Function Deconvolution. Pure Appl. Geophys., 171, 2841–
513 2862. doi:10.1007/s00024-014-0804-0

514 Beresnev, I.A. (2001) What we can and cannot learn about earthquake sources from the spectra
515 of seismic waves. Bull. Seismol. Soc. Am., 91, 397–400, Seismological Society of America.
516 doi:10.1785/0120000115

517 Ben-Menahem, A. (1961) Radiation of seismic surface-waves from finite moving sources. *Bull.*
518 *Seismol. Soc. Am.*, **51**, 401–435, The Seismological Society of America.
519 doi:10.1785/bssa0510030401

520 Bilek, S.L., Lay, T. & Ruff, L.J. (2004) Radiated seismic energy and earthquake source duration
521 variations from teleseismic source time functions for shallow subduction zone thrust
522 earthquakes. *J. Geophys. Res. Solid Earth*, **109**. doi:10.1029/2004JB003039

523 Boore, D.M. (1983) Stochastic simulation of high-frequency ground motions based on
524 seismological models of the radiated spectra. *Bull. Seismol. Soc. Am.*, **73**, 1865–1894.
525 Retrieved from http://www.bssaonline.org/cgi/content/abstract/73/6A/1865

526 Brune JN. (1970) Tectonic stress and the spectra of seismic shear waves from earthquakes. *J*
527 *Geophys Res*, **75**, 4997–5009, Wiley Online Library. doi:10.1029/jb075i026p04997

528 Chounet, A. & Vallée, M. (2018) Global and Interregion Characterization of Subduction
529 Interface Earthquakes Derived From Source Time Functions Properties. *J. Geophys. Res.*
530 *Solid Earth*, **123**, 5831–5852. doi:10.1029/2018jb015932

531 Choy, G.L. & Boatwright, J.L. (1995) Global patterns of radiated seismic energy and apparent
532 stress. *J. Geophys. Res.*, **100**, 18205–18228, Wiley Online Library. doi:10.1029/95jb01969

533 Choy, G.L. & Kirby, S.H. (2004) Apparent stress, fault maturity and seismic hazard for normal-
534 fault earthquakes at subduction zones. *Geophys. J. Int.*, **159**, 991–1012. doi:10.1111/j.1365-
535 246x.2004.02449.x

536 Choy, G.L., McGarr, A., Kirby, S. & Boatwright, J.H. (2006) An overview of the global
537 variability in radiated energy and apparent stress. *Washingt. DC Am. Geophys. Union*
538 *Geophys. Monogr. Ser.*

539 Choy, G.L., McGarr, A., Kirby, S.H. & Boatwright, J. (2013) An Overview of the Global
540 Variability in Radiated Energy and Apparent Stress. in *Earthquakes: Radiated Energy and*
541 *the Physics of Faulting*, Vol. 170, pp. 43–57. doi:10.1029/170GM06

542 Convers, J.A. & Newman, A. V. (2011) Global evaluation of large earthquake energy from 1997
543 through mid-2010. *J. Geophys. Res. Solid Earth*, **116**. doi:10.1029/2010jb007928

544 Das, S. (1988) Relation between average slip and average stress drop for rectangular faults with
545 multiple asperities. *Bull. - Seismol. Soc. Am.*, **78**, 924–930.

546 Denolle, M.A. & Shearer, P.M. (2016) New perspectives on self-similarity for shallow thrust
547 earthquakes. *J. Geophys. Res. Solid Earth*, **121**, 6533–6565. doi:10.1002/2016jb013105

548 Duputel, Z., Tsai, V.C., Rivera, L. & Kanamori, H. (2013) Using centroid time-delays to
549 characterize source durations and identify earthquakes with unique characteristics. *Earth*
550 *Planet. Sci. Lett.*, **374**, 92–100, Elsevier. doi:10.1016/j.epsl.2013.05.024

551 Eshelby, J.D. (1957) The determination of the elastic field of an ellipsoidal inclusion, and related
552 problems. *Proc. R. Soc. Lond. A. Math. Phys. Sci.*, 376–396. doi:10.1098/rspa.1983.0054

553 Fukuyama, E., Ishida, M., Dreger, D.S. & Kawai, H. (1998) Automated Seismic Moment Tensor
554 Determination by Using On-line Broadband Seismic Waveforms. Zisin (Journal Seismol.
555 Soc. Japan. 2nd ser.), 51, 149–156. doi:10.4294/zisin1948.51.1_149

556 Hartzell, S.H. (1978) Earthquake aftershocks as Green's functions. *Geophys. Res. Lett.*, **5**,
557 doi:10.1029/GL005i001p00001

558 Ide, S. & Beroza, G.C. (2001) Does apparent stress vary with earthquake size? *Geophys. Res.*
559 *Lett.*, **28**, 3349–3352. doi:10.1029/2001GL013106

560 Izutani, Y. & Kanamori, H. (2001) Scale-dependence of seismic energy-to-moment ratio for
561 strike-slip earthquakes in Japan. *Geophys. Res. Lett.*, **28**, 4007–4010.
562 doi:10.1029/2001GL013402

563 Izutani, Y. (2005) Radiated energy from the mid Niigata, Japan, earthquake of October 23, 2004,
564 and its aftershocks. Geophys. Res. Lett., 32. doi:10.1029/2005gl024116

565 Izutani, Y. (2008) Radiated energy from the Noto Hanto, Japan, earthquake of March 25, 2007,
566 and its aftershock. *Earth, Planets Sp.*, **60**, 145–150. doi:10.1186/bf03352776

567 Jin, A. & Fukuyama, E. (2005) Seismic Energy for Shallow Earthquakes in Southwest Japan.
568 *Bull. Seismol. Soc. Am.*, **95**, 1314–1333. doi:10.1785/0120040011

569 Jost, M.L., Büßelberg, T., Jost, Ö. & Harjes, H.P. (1998) Source parameters of injection-induced
570 microearthquakes at 9 km depth at the KTB deep drilling site, Germany. *Bull. Seismol. Soc.*
571 *Am.*, **88**, 815–832.

572 Kanamori, H. & Anderson, D. (1975) Theoretical basis of some empirical relations in
573 seismology. *Bull. Seismol. Soc. Am.*, **65**, 1073–1095. Retrieved from
574 http://bssa.geoscienceworld.org/content/65/5/1073.short

575 Kanamori, H. & Heaton, T.H. (2000) Microscopic and Macroscopic Physics of Earthquakes. in
576 GeoComplexity and the Physics of Earthquakes Geophysical Monograph, Vol. 120.

577 Kanamori, H. & Rivera, L. (2004) Static and dynamic scaling relations for earthquakes and their
578 implications for rupture speed and stress drop. *Bull. Seismol. Soc. Am.*, **94**, 314–319,
579 Seismological Society of America.

580 Kanamori, H. & Rivera, L. (2006) Energy partitioning during an earthquake. in *Geophysical*
581 *Monograph Series*, Vol. 170, pp. 3–13. doi:10.1029/170GM03

582 Kanamori, H. & Ross, Z.E. (2019) Reviving mB. *Geophys. J. Int.*, **216**, 1798–1816, Oxford
583 University Press. doi:10.1093/gji/ggy510

584 Kanamori, H., Mori, J., Hauksson, E., Heaton, T.H., Hutton, L.K. & Jones, L.M. (1993)
585 Determination of earthquake energy release and ML using TERRAscope. *Bull. - Seismol.*
586 *Soc. Am.*, **83**, 330–346, The Seismological Society of America.

587 Kanamori, H., Ross, Z.E. & Rivera, L. (2020) Estimation of radiated energy using the KiK-net
588 downhole records - Old method for modern data. *Geophys. J. Int.*, **221**, 1029–1042, Oxford
589 University Press. doi:10.1093/gji/ggaa040

590 Kikuchi, M. & Kanamori, H. (1982) Inversion of complex body waves -. *Bull. - Seismol. Soc.*
591 *Am.*, **72**, 491–506. doi:10.1785/bssa0810062335

592 Ligorría, J.P. & Ammon, C.J. (1999) Iterative deconvolution and receiver-function estimation.
593 *Bull. Seismol. Soc. Am.*, **89**, 1395–1400.

594 Madariaga, R. & Ruiz, S. (2016) Earthquake dynamics on circular faults: a review 1970–2015. *J.*
595 *Seismol.*, **20**, 1235–1252. doi:10.1007/s10950-016-9590-8

596 Malagnini, L., Scognamiglio, L., Mercuri, A., Akinci, A. & Mayeda, K. (2008) Strong evidence
597 for non-similar earthquake source scaling in central Italy. *Geophys. Res. Lett.*, **35**.
598 doi:10.1029/2008gl034310

599 Malagnini, L., Mayeda, K., Nielsen, S., Yoo, S.-H., Munafo', I., Rawles, C. & Boschi, E. (2014)
600 Scaling Transition in Earthquake Sources: A Possible Link Between Seismic and
601 Laboratory Measurements. *Pure Appl. Geophys.*, **171**, 2685–2707. doi:10.1007/s00024-013-
602 0749-8

603 Mayeda, K. & Walter, W.R. (1996) Moment, energy, stress drop, and source spectra of western
604 United States earthquakes from regional coda envelopes. *J. Geophys. Res. B Solid Earth*,
605 **101**, 11195–11208, Wiley Online Library. doi:10.1029/96jb00112

606 Mayeda, K., Gök, R., Walter, W.R. & Hofstetter, A. (2005) Evidence for non-constant
607 energy/moment scaling from coda-derived source spectra. *Geophys. Res. Lett.*, **32**, 1–4.
608 doi:10.1029/2005GL022405

609 Mori, J., Abercrombie, R.E. & Kanamori, H. (2003) Stress drops and radiated energies of
610 aftershocks of the 1994 Northridge, California, earthquake. *J. Geophys. Res. Solid Earth*,
611 **108**. doi:10.1029/2001jb000474

612 Newman, A. V & Okal, E.A. (1998) Teleseismic estimates of radiated seismic energy: The E/M
613 0 discriminant for tsunami earthquakes. *J. Geophys. Res. Solid Earth*, **103**, 26885–26898,
614 Wiley Online Library. doi:10.1029/98jb02236

615 Nishitsuji, Y. & Mori, J. (2014) Source parameters and radiation efficiency for intermediate-
616 depth earthquakes in Northeast Japan. *Geophys. J. Int.*, **196**, 1247–1259.
617 doi:10.1093/gji/ggt458

618 NIED. (2019a) NIED Hi-net, National Research Institute for Earth Science and Disaster
619 Resilience. doi:10.17598/NIED.0003

620 NIED. (2019b) NIED F-net, National Research Institute for Earth Science and Disaster
621 Resilience. doi:10.17598/NIED.0005

622 NIED. (2019c) NIED V-net, National Research Institute for Earth Science and Disaster
623 Resilience. doi:10.17598/NIED.0006

624 NIED. (2019d) NIED K-NET, KiK-net, National Research Institute for Earth Science and
625 Disaster Resilience. doi:10.17598/NIED.0004

626 Pérez-Campos, X. & Beroza, G.C. (2001) An apparent mechanism dependence of radiated
627 seismic energy. *J. Geophys. Res. Solid Earth*, **106**, 11127–11136, Wiley Online Library.
628 doi:10.1029/2000jb900455

629 Prejean, S.G. & Ellsworth, W.L. (2001) Observations of Earthquake Source Parameters at 2 km
630 Depth in the Long Valley Caldera, Eastern California. *Bull. Seismol. Soc. Am.*, **91**, 165–177.
631 doi:10.1785/0120000079

632 Prieto, G.A., Parker, R.L. & Vernon, F.L. (2009) A Fortran 90 library for multitaper spectrum
633 analysis. *Comput. Geosci.*, **35**, 1701–1710. doi:10.1016/j.cageo.2008.06.007

634 Ross, Z.E., Kanamori, H., Hauksson, E. & Aso, N. (2018) Dissipative Intraplate Faulting During
635 the 2016 Mw 6.2 Tottori, Japan Earthquake. J. Geophys. Res. Solid Earth, 123, 1631–1642,
636 Wiley Online Library. doi:10.1002/2017JB015077

637 Rudnicki, J.W. & Kanamori, H. (1981) Effects of fault interaction on moment, stress drop, and
638 strain energy release. *J. Geophys. Res. Solid Earth*, **86**, 1785–1793.
639 doi:10.1029/jb086ib03p01785

640 Shearer, P.M., Prieto, G.A. & Hauksson, E. (2006) Comprehensive analysis of earthquake source
641 spectra in southern California. J. Geophys. Res. Solid Earth, **111**, 6.
642 doi:10.1029/2005JB003979

643 Singh, S.K. & Ordaz, M. (1994) Seismic energy release in Mexican subduction zone
644 earthquakes. *Bull. - Seismol. Soc. Am.*, **84**, 1533–1550.

645 Takahashi, T., Sato, H., Ohtake, M. & Obara, K. (2005) Scale dependence of apparent stress for
646 earthquakes along the subducting pacific plate in northeastern Honshu, Japan. *Bull. Seismol.*
647 *Soc. Am.*, **95**, 1334–1345. doi:10.1785/0120040075

648 Thomson, D.J. (1982) Spectrum Estimation and Harmonic Analysis. *Proc. IEEE*, **70**, 1055–
649 1096. doi:10.1109/PROC.1982.12433

650 Ueno, H., Hatakeyama, S., Aketagawa, T., Funasaki, J. & Hamada, N. (2002) Improvement of
651 hypocenter determination procedures in the japan meteorological agency. *Q. J. Seism*, **65**,
652 123–134.

653 Vassiliou, M.S. & Kanamori, H. (1982) The energy release in earthquakes. *Bull. Seismol. Soc.*
654 *Am.*, **72**, 371–387.

655 Venkataraman, A. & Kanamori, H. (2004) Observational constraints on the fracture energy of
656 subduction zone earthquakes. *J. Geophys. Res. Solid Earth*, **109**.
657 doi:10.1029/2003JB002549

658 Wyss, M. (1970) Apparent Stresses of Earthquakes on Ridges compared to Apparent Stresses of
659 Earthquakes in Trenches. Geophys. J. R. Astron. Soc., 19, 479–484. doi:10.1111/j.1365-
660 246x.1970.tb00153.x

661 Wyss, M. & Brune, J.N. (1968) Seismic moment, stress, and source dimensions for earthquakes
662 in the California-Nevada region. J. Geophys. Res., 73, 4681−4694.
663 doi:10.1029/jb073i014p04681

664 Ye, L., Lay, T. & Kanamori, H. (2013) Ground shaking and seismic source spectra for large
665 earthquakes around the megathrust fault offshore of northeastern Honshu, Japan. Bull.
666 Seismol. Soc. Am., 103, 1221–1241, Seismological Society of America.

667 Ye, L., Lay, T., Kanamori, H. & Rivera, L. (2016a) Rupture characteristics of major and great
668 (Mw ≥ 7.0) megathrust earthquakes from 1990 to 2015: 2. Depth dependence. *J. Geophys.*
669 *Res. Solid Earth*, **121**, 845–863, Wiley Online Library. doi:10.1002/2015JB012427

670 Ye, L., Lay, T., Kanamori, H. & Rivera, L. (2016b) Rupture characteristics of major and great
671 (Mw ≥ 7.0) megathrust earthquakes from 1990 to 2015: 1. Source parameter scaling
672 relationships. *J. Geophys. Res. Solid Earth*. doi:10.1002/2015JB012426

673 Ye, L., Kanamori, H. & Lay, T. (2018) Global variations of large megathrust earthquake rupture
674 characteristics. *Sci. Adv.*, **4**, eaao4915, American Association for the Advancement of
675 Science. doi:10.1126/sciadv.aao4915

Yoshida, K. (2019) Prevalence of asymmetrical rupture in small earthquakes and its effect on the estimation of stress drop: a systematic investigation in inland Japan. *Geosci. Lett.*, **6**. doi:10.1186/s40562-019-0145-z

Yoshida, K., Taira, T., Matsumoto, Y., Saito, T., Emoto, K. & Matsuzawa, T. (2020) Stress Release Process Along an Intraplate Fault Analogous to the Plate Boundary: A Case Study of the 2017 M5.2 Akita-Daisen Earthquake, NE Japan. *J. Geophys. Res. Solid Earth*, **125**. doi:10.1029/2020JB019527

Zollo, A., Orefice, A. & Convertito, V. (2014) Source parameter scaling and radiation efficiency of microearthquakes along the Irpinia fault zone in southern Apennines, Italy. *J. Geophys. Res. Solid Earth*, **119**, 3256–3275. doi:10.1002/2013jb010116

Appendix A- Frequently used symbols and relationships

Symbols

M_0 seismic moment

E_R radiated energy

e_R scaled energy

ρ, α, β, μ medium parameters. Density, P-wave velocity, S-wave velocity, shear modulus.

f_c corner frequency of the ω^2-model

T duration of the moment rate function

$$T = \frac{2}{\pi f_c} \text{ (triangle), } T = \frac{5}{2\pi f_c} \text{ (truncated } t\exp\left(-t/2\pi f_c\right)$$

$REEF$ (R) radiated energy enhancement factor

$\Delta\sigma$ static stress drop, stress parameter

η_R radiation efficiency

a radius of a circular fault

c constant relating f_c to the radius of a circular fault

Relationships

(A1) $e_R \equiv \frac{E_R}{M_0} = \frac{\pi^2}{5}\left(\frac{M_0 f_c^3}{\rho\beta^5}\right)$ for the ω^2-model (P-wave energy ignored)

(A2) $T = \frac{2}{\pi f_c}$ (for an isosceles triangle), $T = \frac{5}{2\pi f_c}$ (for the truncated $t\exp\left(-t/2\pi f_c\right)$)

(A3) $e_R = \frac{E_R}{M_0} = \frac{25}{8\pi}\left(\frac{M_0}{\mu\beta^3 T^3}\right)$ similar to (A1) but with T instead of f_c (for the truncated exponential MRF)

709 (A4) $REEF = \frac{5\pi}{6}\left(\frac{E_R}{M_0}\right)\left(\frac{\mu\beta^3 T^3}{M_0}\right)$ definition of *REEF*

710 (A5) $M_0 = \frac{16}{7}a^3\Delta\sigma$ for a circular fault, static relation

711 (A6) $f_c = \frac{c}{2\pi}\frac{\beta}{a}$

712 Brune's (1970) heuristic relation partially based on energy conservation (c=2.34).

713 (A7) $f_c = \frac{c}{2\pi}\beta\left(\frac{16}{7}\frac{\Delta\sigma}{M_0}\right)^{1/3}$ from (A5) and (A6)

714 (A8) $\Delta\sigma = \left(\frac{7\pi^3}{2c^3}\right)\mu\left(\frac{M_0 f_c^3}{\mu\beta^3}\right)$ relation for the ω^2 model with the Brune's constant c

715 (A8') $\Delta\sigma = \left(\frac{875}{16c^3}\right)\mu\left(\frac{M_0}{\mu\beta^3 T^3}\right)$ same as above for a truncated exponential MRF

716

717 **Data availability**

718 This study used hypocentres and S-wave arrival time data reported in the JMA unified catalogue.

719 The seismograms were collected and stored by the JMA, national universities, and NIED

720 (http://www.hinet.bosai.go.jp/?LANG=en).

721